Research Article Vol. 2, No. 6 / 15 June 2019 / OSA Continuum 1982
OSA CONTINUUM

Plasmon antenna array "patchwork" lasers — towards low etendue, speckle free light sources

KE GUO, SACHIN KASTURE, AND A. FEMIUS KOENDERINK*

Center for Nanophotonics, AMOLF, Science Park 104, 1098 XG, Amsterdam, The Netherlands
**f.koenderink@amolf.nl*

Abstract: In this work, we study plasmon antenna array lasers for solid-state lighting (SSL). Optically pumped plasmon antenna array lasers can provide benefits suitable for SSL including efficient pump-light absorption, high brightness, and good directivity. However, applying lasers in SSL is difficult because of speckle formation. To overcome this issue, we propose two types of lasers based on patchworks of small plasmon lattices with different lattice constants, tessellating an extended surface. The premise is that they could ultimately form a blue-LED pumped broad-area directional emitter with reduced coherence to suppress speckle. An important question is whether different patches couple when assembled together, and how this affects spatial and spectral profiles. In this paper, we show measurement results on the plasmon patchwork lasers, and discuss their modelling and potential application as low etendue and speckle free sources in SSL.

1. Introduction

Lasers are relevant for solid-state lighting (SSL) either as pump sources for phosphors in laser-driven white light sources [1–3], or as illumination sources in applications like projection [4] that require both high power and a low etendue. For instance, projection with digital mirror device beam scanning of red, green and blue laser channels offers superior projection brightness and reduced maintenance compared to lamps [5]. However, speckle forms a challenge for lasers. Speckles are high contrast random interference patterns which occur due to high temporal and spatial coherence of lasers [6]. To reduce speckle contrast a variety of methods have been developed based on superimposing statistically independent speckle configurations. This includes using (multiple) sources with different wavelengths, illumination angles and polarizations [7,8], reducing spatial coherence of sources [9], and dynamically changing the illumination or target screen [10–13]. Most of these methods require multiple light sources, bulky optics and/or mechanical driving of, e.g., spinning diffusers. A compact laser with effectively low spatial and temporal coherence emission could be desirable for creating small, speckle free projection systems.

We explore the possibility of using distributed feedback (DFB) lasers based on arrays of plasmonic nanoparticles [14–24]. Benefiting from the strong plasmon resonance of the arrays, they feature the possibility of lasing from a very small sample area, and "flat-optics" control of frequency and emission pattern through array patterning [25–27]. Furthermore, they have a geometry similar to plasmon-array enhanced remote phosphor structures, which were already explored for blue-LED pumped bright white light fluorescence [28,29], showing advantages in terms of high pump-light absorption and internal quantum efficiency. One could thus envision blue-LED pumped plasmonic laser substrates that multiplex many plasmon lasers, and thereby tailor functions in the spatial, spectral, and wave vector domain. In this paper, we consider the possibility of making multi-wavelength, low etendue, yet low-speckle plasmon DFB lasers based on so-called patchwork arrays. We introduce two types of arrays: "checkerboards" and "random patchworks". Both are patchworks of small plasmon lattices, each of which can operate individually as a DFB laser, similar to the ones studied in Ref. [20]. The patchworks are similar

#362014 https://doi.org/10.1364/OSAC.2.001982
Journal © 2019 Received 8 Mar 2019; revised 14 May 2019; accepted 20 May 2019; published 12 Jun 2019

OSA CONTINUUM

to the plasmon particle superlattices studied by Wang et al. [27]. However, in contrast to their work, the patchwork arrays we investigate feature different pitches in different patches, and smaller inter-patch distances (a few hundred nm compared with a few micron in Ref. [27]). Open questions are if these lasers will operate independently when assembled together, or whether different patches will couple to each other, thereby giving rise to different lasing phenomena. We measure the lasing properties of these patchwork lasers, including the lasing threshold, spectra, and angular distribution of lasing emission. The lasers exhibit multiple lasing modes simultaneously at different frequencies. To understand the origin of multi-mode lasing observed in these systems, we investigate a DFB laser dimer consisting of two interacting DFB lasers. Furthermore, we propose an extension of coupled wave theory to explain the large number of modes observed.

2. Sample geometries

Fig. 1 illustrates two distinct patchwork design families. Both start from a square array of $N \times N$ particles (Ag disks) with pitch $d = 370$ nm, deposited on glass and embedded in a ca. 350 nm thick spincoated SU8 layer of index 1.60 that provides gain by doping with laser dye (Rh6G at 2.5 wt%). This layer forms a 2D waveguide with single TE (with in-plane electric field perpendicular to the propagation direction) and TM modes (with mainly out-of-plane electric field) with index $n_{WG} \approx 1.55$. Earlier works [20,26] show that the waveguide modes can couple with each other through the Bragg diffractions of order (±2,0) and (0,±2) of the arrays while being amplified by the gain medium (the Rh6G doped SU8 waveguide), resulting in lasing at $\lambda_0 \approx 574$ nm ($\omega_0 \approx 3.28 \times 10^{15}$ rad/s). These lasing modes are then coupled out through Bragg diffractions of order (±1,0) and (0,±1) into the direction nearly normal to the waveguide plane. We create patchworks by dividing the array into sub-arrays of size $n \times n$, with the quotient $m = N/n$ an integer. The first design is a "checkerboard", in which alternating arrays are of type A (unchanged), or type B of which the pitch is increased to $d' = d + \delta$, while keeping the center position. To avoid overlapping of particles, we reduce the number of particles in the B arrays to fit within their original bounding box. Effectively this design results in a 45 degree rotated super-square-lattice of A and B patches with a period of $\sqrt{2}n \cdot d$. In this paper, we consider $N = 240$ and $n = 10, 20, 40, 60$, and $\delta = 1, 2, 4$ nm, in which case the B patches have $(n-1) \times (n-1)$ particles and are shifted by $d/2$ from the original patches.

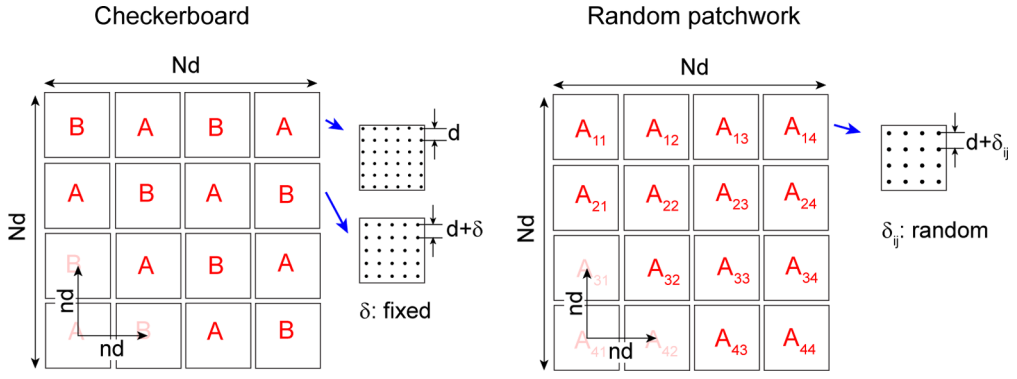

Fig. 1. A schematic of the sample design. An $N \times N$ square array is divided into patches of $n \times n$. To make a checkerboard array, we change the pitch of the B patches from d to $d + \delta$. The particle numbers are reduced so that the resulting B' patches are not larger than the original B patches. For the Random patchwork arrays, we change the pitches in every patch to $d + \delta_{ij}$ and also change the particle numbers accordingly to fit in the original patch size.

OSA CONTINUUM

The second sample family is a "randomized patchwork". Each sub-array i, j is expanded or shrunken by adding a random number δ_{ij} (uniformly distributed over $[-\delta, \delta]$) to the pitch, where we again apply centering and clipping. The result is a patch work of sub-arrays of different pitches, with their centers fixed in a square lattice with period $n \cdot d$. We perform experiments taking $N = 240$, and varying n, as well as the randomization range $\delta = 1, 2, 4, 10$ nm. The δ_{ij} are set as random integer multiples of 0.2 nm, which is the lithography step size. The designs are implemented with electron beam lithography and lift-off [20,25,26], leading to Ag nanoparticles of cylindrical shape with a diameter of about 60 nm and a height of 30 nm.

3. Fourier analysis

For simple plasmon array lasers a first order approximation to the band structure is the nearly free photon dispersion [20,26], which can be obtained by convolving the array Fourier transform, with the waveguide dispersion relation (the locus of points in k-space $|\mathbf{k}_{||}| = (\omega/c)n_{\mathrm{WG}}$). Crossings in this bandstructure will typically lead to stop gaps and lasing conditions. Once lasing is achieved, typically at the Γ-point of the band structure, the output pattern essentially copies the array Fourier transform [26]. On this basis we envision two distinct scenarios that may describe the patchworks. Firstly, one can envision that the patchworks would support extended lasing modes, and the Fourier analysis outlined above, applied to the entire patchwork, would predict lasing conditions and radiation patterns. Alternatively, if patches should be viewed as uncoupled, one would expect output to be the incoherent sum of emission from individual arrays, at multiple wavelengths (two for the checkerboard, of order $(N/n)^2$ for the random patchworks) determined by the different lattice pitches. In this second scenario, the small size of the patches would adversely affect threshold gain and raise output etendue compared with a full-sized square array.

In the following, we examine the Fourier transforms of the checkerboard and random patchworks and estimate the resulting nearly-free-photon band structures. As an example, consider the Fourier transform of a checkerboard array with $n = 10$, $\delta = 1$ nm. The array can be viewed as a square superlattice with pitch $\sqrt{2}nd$ rotated by 45° and convolved with a dimer of neighbouring A and B arrays. According to the convolution theorem, its structure factor (Fourier transform) is the product of the Fourier transform of the superlattice, i.e., a 45° rotated square lattice with pitch $G/(\sqrt{2}n)$ (defining $G = 2\pi/d$), and that of an A-B dimer. The Fourier transform of an A-B dimer is shown in Fig. 2(a). The final result (Fig. 2(b)) is a group of distinct reciprocal space maxima near $(\pm 1, 0)G$ and $(0, \pm 1)G$, at $(\pm 1, 0)G + (i, j)G/(2n)$ and $(0, \pm 1)G + (i, j)G/(2n)$, with $i, j = 0, \pm 1, ...$ Particularly, four peaks are pronounced in each of the groups, i.e., $(\pm 1, 0)G + (\pm 1, \pm 1)G/(2n)$ or $(0, \pm 1)G + (\pm 1, \pm 1)G/(2n)$. The locations of the peaks are set by the lattice constant of the superlattice, i.e., $\sqrt{2}nd$. On the other hand, δ only affects the A-B dimer and hence the amplitude of the peaks. Figure 2(c) shows the Fourier transforms from a lattice with $n = 40$. The resulting bandstructures are obtained by convolution with the waveguide dispersion, which consists of multiple cones in $k_x - k_y - \omega$ space. Figure 2(d) illustrates a constant frequency cut of the band structure of a checkerboard with $n = 10$ and $\delta = 1$ nm at ω_0. The waveguide modes at ω_0 with wave vector of $(\pm 1, 0)G$ and $(0, \pm 1)G$ can couple with each other through the diffraction at $(\pm 1, 0)G + (\pm 1, \pm 1)G/(2n)$ and $(0, \pm 1)G + (\pm 1, \pm 1)G/(2n)$, and can be coupled out with wave vector of $(\pm 1, \pm 1)G/2n$. Therefore, the most pronounced bands (indicated by red dashed lines) cross at $(\pm 1, \pm 1)G/2n$ in Fig. 2(d). Figure 2(e-f) illustrate the band structures of a checkerboard with $n = 10, 40$, $\delta = 1$ nm, at $k_y = 0$. When $n = 10$, instead of two straight lines and a parabolic crossing at ω_0 and $k_x = 0$ expected for simple square lattices [20], the band structure of the checkerboard arrays shows four linear bands intersecting at two points at $\omega \approx \omega_0$. These result from shifting the bands of a square lattice by $(\pm 1, \pm 1)G/(2n)$ in Fourier space. The parabolas are also shifted in both frequency and $\boldsymbol{k}$. As n increases to 40, the straight bands converge to the two straight bands of a square array.

OSA CONTINUUM

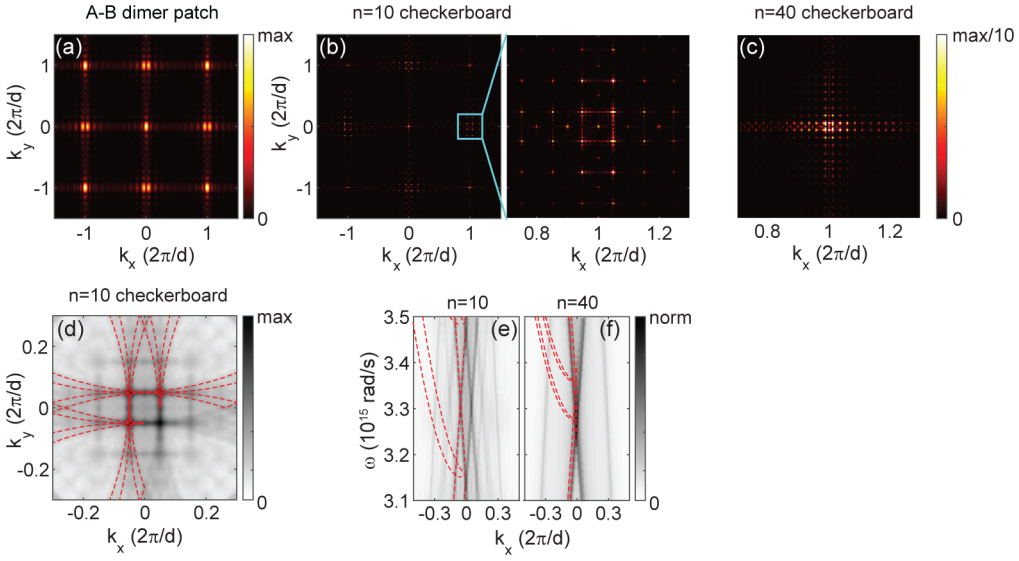

Fig. 2. (a) Calculated absolute value of Fourier transform of a A-B' dimer with $n = 10$ and $\delta = 1$ nm. (b) Calculated absolute value of Fourier transform of a checkerboard laser with $n = 10$ and $\delta = 1$ nm (left). Groups of peaks occur near the base lattice reciprocal lattice vectors $(\pm 1, 0)G$ and $(0, \pm 1)G$ (right shows zoom). (c) similar zoom of Fourier transform of a checkerboard laser with $n = 40$, showing that the supercell features come closer together. (b-c) are normalized to $1/10$ of the maximum at $k_x = k_y = 0$. (d-e) Calculated band structures of checkerboard lasers with $\delta = 1$ nm at (d) ω_0 and (e-f) $k_y = 0$ for (e) $n = 10$ and (f) $n = 40$, obtained by convolving the structure factor with the 'free photon' waveguide dispersion. Red lines indicate dominant features expected taking just dominant peaks in the structure factor.

We apply similar Fourier transform methodology to random patchwork laser, averaging over 20 different random realizations for an ensemble average estimate. Similar to simple square lattices, the structure factors feature high intensity near $(\pm 1, 0)G$ and $(0, \pm 1)G$. Zooming in on one diffraction order as example ($(1, 0)G$ in Fig. 3(a)), we find that the randomization of pitch broadens the diffraction order (sinc-type broadening expected for small patches) compared to the simple square array. Moreover, since the A_{ij} arrays are arranged on a square superlattice, diffraction peaks appear closely spaced at $(1, 0)G + (i, j)G/n$ with $i, j = 0, \pm 1, \pm 1, \ldots$. Figure 3(b) shows the predicted band structures for the TE modes at $k_y = 0$ for $n = 10$ and 40. The broadening of the Fourier transform near $(\pm 1, 0)G$ and $(0, \pm 1)G$ results in a blurring of the bands. When $n = 10$, the band structure appear as one major broad band near $k_x = k_y = 0$. At $n = 40$, the random patchwork has similar band structure as a square array. To sum up, the random patchwork lasers are expected to have access to a range of Bragg conditions, suggesting that lasing may involve a distribution of spectral components and output wave vectors.

OSA CONTINUUM

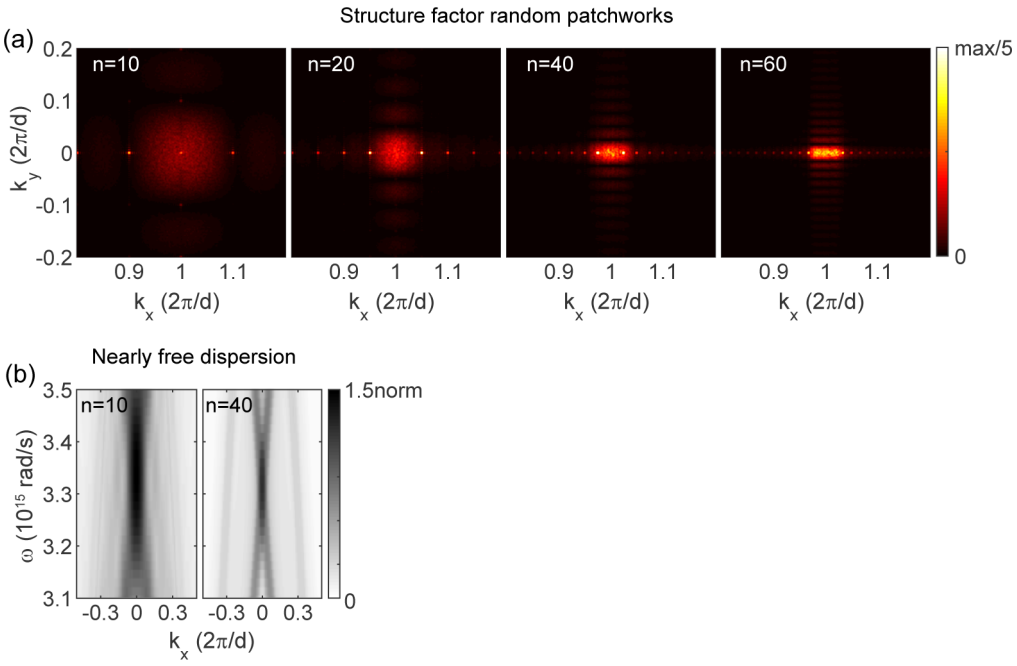

Fig. 3. (a) Calculated root mean square of Fourier transforms of 20 realizations of random patchwork lasers with $n = 10, 20, 40, 60$ and $|\delta_{ij}|$<10 nm near $(G, 0)$. All images are normalized to $1/5$ of the maximum at $k_x = k_y = 0$. (b) Calculated band structures of random patchwork arrays with $n = 10$, 40 and $|\delta_{ij}|$<10 nm. They are normalized to 1.5 times the normalization factor (norm) in Fig. 2(g).

4. Results

In this section, we report measurements of basic optical properties of the checkerboard and the random patchwork lasers. We use the experimental set up discussed in earlier works [20,30] for spectrally resolved Fourier and real-space imaging, using single shot pulsed excitation with 0.5 ns pulses at 532 nm, and a 50 × microscope objective of NA=0.7 (Nikon L PLAN) chosen for a large field of view. First, we check the Fourier analysis by measuring the (below threshold) band structure of the arrays. Second, through pump power dependent output measurements, we study the lasing threshold and lasing spectra. To interpret the measurement results, we look into the emergence of multiple lasing modes from coupled patches using coupled wave theory. Finally, we study the angular distribution by measuring the Fourier space images.

4.1. Band structure measurements

We measure the below threshold band structures of the checkerboard and random patchwork arrays through spectrally resolved Fourier imaging at low power. As shown in Fig. 4(a), the checkerboard array with $n = 10$ has four bands crossing at finite k_x near $\omega \approx 3.31 \times 10^{15}$ rad/s, similar to the prediction in Fig. 2(e). As n increases to 40, the band structure converges to that of a square array. The random patchwork with $n = 10$ has a broad band near $k_x = 0$ (Fig. 4(b)). When $n = 40$, the broad feature narrows into the two straight bands also expected for a simple square lattice. We are not able to recognize the parabolic band predicted by the calculation as it is too weak. To sum up, the measured band structures of both checkerboard and random patch work lasers show qualitative agreement with the predictions in Fig. 2 and 3. These observations indicate that the below-threshold emission arises from emission into waveguide modes, coupled

OSA CONTINUUM

out by diffraction. Upon outcoupling the diffraction pattern of the full array structure is imparted to the output, consistent with fluorescence studies on a plethora of other systems with 2D particle assemblies in fluorescent waveguide layers, including Vogel spirals and aperiodic lattices [26,31].

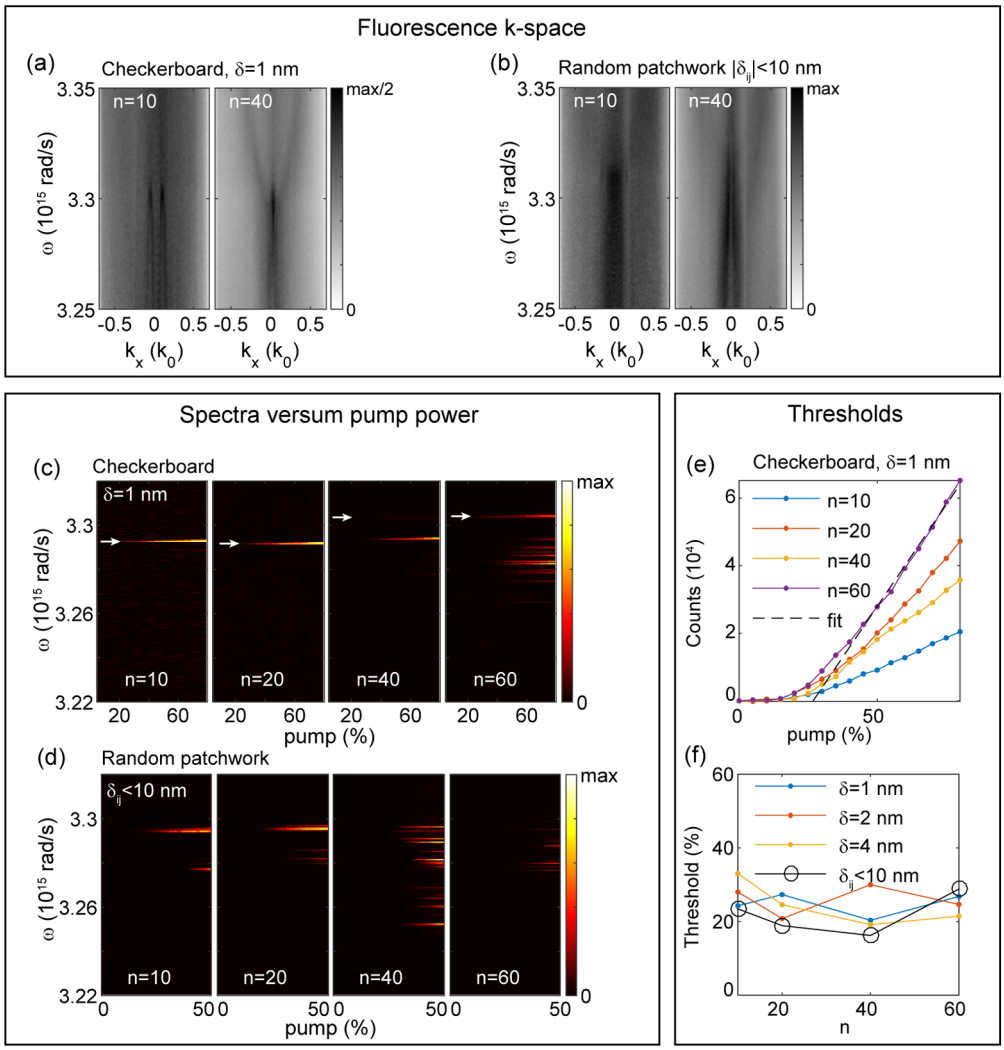

Fig. 4. Measured band structures at $k_y = 0$ of (a) checkerboard and (b) random patchwork lasers with $n = 10, 40, 60$, $\delta = 1$ nm and $|\delta_{ij}|<5$ nm. The images are obtained by dividing the spectrometer camera images by the corresponding spectra (sum over k_x) along the frequency direction for optimum contrast. The resulting images are normalized to the maxima or half maxima of each image. (a) is obtained with 1000 pulses at 7 % pump power. (b) is obtained with 1000 pulses at 10 % pump power.(c) Measured spectra at $k_x = 0$ of checkerboard lasers as a function of pump power. $n = 10$, 20, 40 and 60, δ=1 nm, (d) Measured spectra at $k_y = 0$ of random patchwork lasers as a function of pump power. $n = 10$, 20, 40 and 60, $\delta_{ij}<10$ nm. (c-d) are normalized to the maxima of each image. (e) Emission intensity at $k_x = 0$ as a function of pump power of the lowest threshold lasing mode measured from checkerboard lasers with $n = 10$, 20, 40, 60, and δ=1 nm. (f) Lasing thresholds of the lowest threshold modes of checkerboard and random patchwork lasers, with $n = 10$, 20, 40, 60, δ=1, 2, 4 nm for the checkerboard lasers and $\delta_{ij}<10$ nm for the random patchwork lasers. White arrows point at the lowest threshold lasing mode.

OSA CONTINUUM

4.2. Lasing thresholds and frequencies

Next, we study the input-output behavior of the lasers by measuring spectra as function of input pulse energy, where the input pulse energy is controlled using a computer-controlled acousto-optical modulator (AOM). The maximum pulse energy corresponds to about 1μJ over an approximately 120 μm wide spot, slightly overfilling the patchwork arrays. The spectrometer collects emission near $k_y = 0$ with a 10 μm slit. Summing over all k_x, we obtain emission spectra. Figure 4(c) shows emission spectra from single shot excitation versus pump power on checkerboard lasers with $n = 10, 20, 40, 60$, and δ=1 nm. All checkerboard arrays show sharp emission peaks (width<0.5 nm, spectrometer limited) starting from a threshold at about 20 % of the maximum pulse energy. Similar multimode lasing with similar thresholds occurs in random patchwork lasers with $n = 10, 20, 40, 60$, and $\delta_{ij} \leq 10$ nm, shown in Fig. 4(d). To confirm that these peaks are indeed lasing modes, we check their threshold behavior. For each sample, we select the mode that emerges at lowest pump power (indicated by the white arrows in Fig. 4(c)) and plot emission intensity within 0.5 nm of the peak wavelength versus pump power (Fig. 4(e)). All plotted modes have distinct threshold behavior, which together with the narrow spectral width confirms lasing. Fitting the input-output curves to linear functions (black dashed line in Fig. 4(e)), we obtain the lasing threshold for checkerboard lasers with $\delta = 1, 2, 4$ nm and for the random patch lasers with biggest disorder $\delta_{ij} \leq 10$ nm, as plotted in Fig. 4(f). The measured lasers all have thresholds well within a factor 2 of those of simple plasmon DFB lasers of the same N [20]. This is remarkable since these thresholds are much lower than the threshold of single patches of size n (e.g., an isolated $N = 60$ patch requires twice the threshold of any investigated patchwork). This finding suggests that lasing modes span multiple patches. We note that the different slope efficiencies in Fig. 4(e), spread by a factor ~ 3, are not necessarily representative of actual slope efficiencies, as our detection scheme implies a filtering in wave vector space (spectrometer slit selects $k_y = 0$).

From Fig. 4(c-d) we conclude that both checkerboard and random patchwork lasers have multiple lasing modes at different frequencies. We recall the two distinct scenarios hypothesized earlier. If all the patches were independent, the checkerboard lasers would have 2 laser lines that are separated by $n_{wg}\delta$, corresponding to about 1.6, 3.1 and 6.2 nm for $\delta = 1, 2, 4$ nm. The random patchwork lasers would have $(N/n)^2$ laser lines spanning over a wavelength range of 31 nm for -10 nm$<\delta_{ij}<10$ nm near the original lasing wavelength λ_0. In the second scenario where all patches are coupled, the checkerboard lasers would likely have one clearly dominant lasing mode at λ_0 where the superlattice bands cross, while the random patchwork lasers would likely have multiple lines near λ_0.

Figure 5(a-c) show above-threshold spectra from the checkerboard lasers with $n = 10$, 20, 40, 60, and $\delta = 1, 2, 4$ nm. The red bars on the top left indicates the expected 1.6, 3.1 and 6.2 nm lasing wavelength range, defined as the range spanned by the geometrical Bragg diffraction conditions corresponding to the pitches in the system. When $n = 10$, the checkerboard lasers tend to emit at one dominant wavelength. This indicates that the checkerboard lasers have a lasing mode that is coherent over the entire array instead of having two sets of patches lasing independently at two frequencies. As n and δ increase, multiple lasing modes (4 to 10 modes) with comparable intensity emerges over a spectral range of 5 to 10 nm. This is not expected from either independent-patch or coupled-patch scenarios. There is a small (a few nm) red shift of the lasing spectra as δ increase from 1 nm to 4 nm, consistent with the fact that average particle distance increases with increasing δ in the checkerboard arrays.

The random patchworks show lasing at multiple wavelengths (2 to 15 lines) within a similar 10 nm band as shown in Fig. 5(d). The number of lasing modes does not increase with decreasing n, i.e., they are not proportional to the number of patches $(N/n)^2$. The total wavelength range spanned by the lasing lines is much smaller than the 31 nm bandwidth, which would be expected if patches would be uncoupled. Together these observations indicate that the individual patches

OSA CONTINUUM

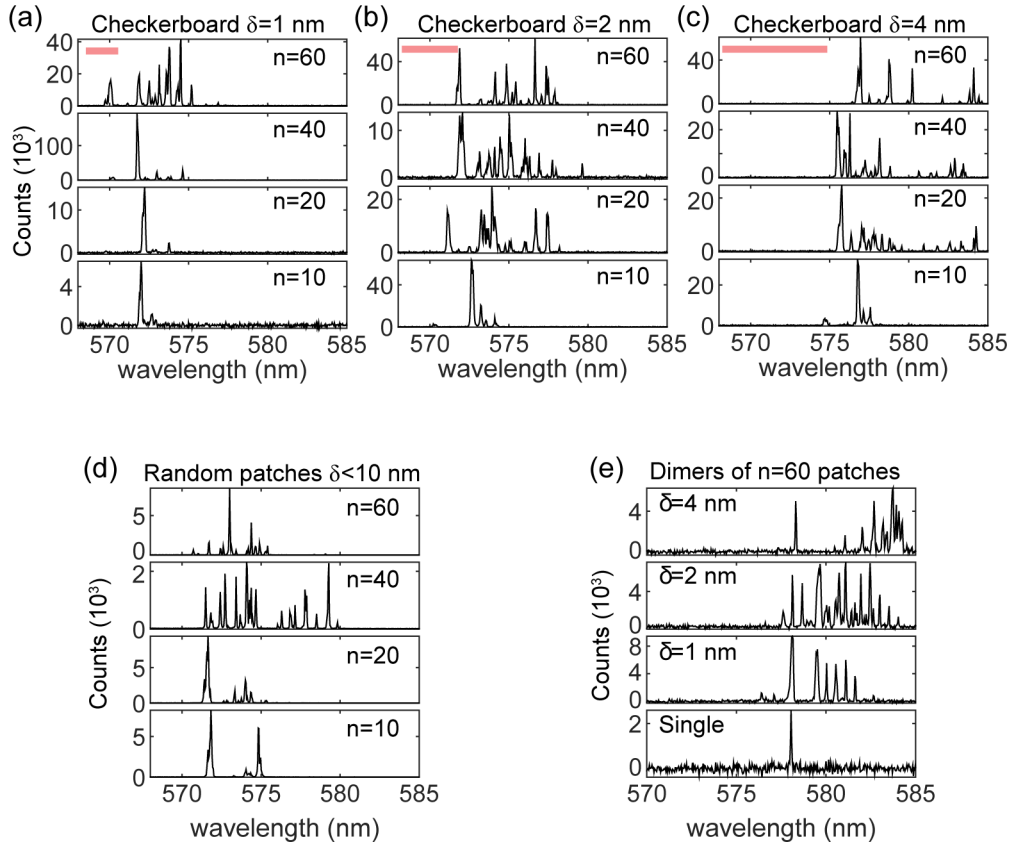

Fig. 5. (a-c) Measured above threshold lasing spectra of checkerboard lasers at 60% pump power. n = 10, 20, 40, 60. (a) δ = 1 nm, (b) δ = 2 nm (c) δ = 4 nm. (d) Measured above threshold lasing spectra of random patchwork lasers at 50% pump power. n = 10, 20, 40, 60, and δ_{ij}<10 nm. (e) Measured above threshold spectra of dimers of two n = 60 patches spaced by 370 nm, and with δ = 1, 2, 4 nm, compared with spectrum of a single patch excited in a checkerboard array with δ = 4 nm and n = 60.

in a random patchwork laser do not act as independent lasers, and lasing arises from coherently coupled patches, as in the checkerboard case.

4.3. *Multi-mode lasing due to coupling of patches*

In the previous section, we have observed two interesting properties of the investigated lasers. First, the measured lasing thresholds are significantly below that of the constituent single patches, indicating that the lasing modes extend over multiple patches or the entire array. This hypothesis is supported by real-space spectral imaging and coherence measurements as shown in Fig. 6. In real space spectral imaging, we project real space images of lasing patchworks onto the 10 μm wide spectrometer slit, to resolve the spectral distribution of light across a diffraction limited line-cut along the entire patchwork length. Figure 6(a) suggests that checkerboard lasers of different δ have lasing modes that extend over the entire patchwork length, apparent as bright lines at constant frequency with intensity variations on different patches. We conduct double slit experiments on the extended lasing modes to check their spatial coherence. To do so, we employ spectral Fourier imaging while selecting two 2 μm stripes on opposing ends of a patchwork using a chrome slit-mask in an intermediate real-space image plane. Figure 6(a) shows an example

OSA CONTINUUM

of measured fringe pattern with contrast limited by unequal stripe intensity, which confirms coherence. Similar results are obtained from random patchwork lasers.

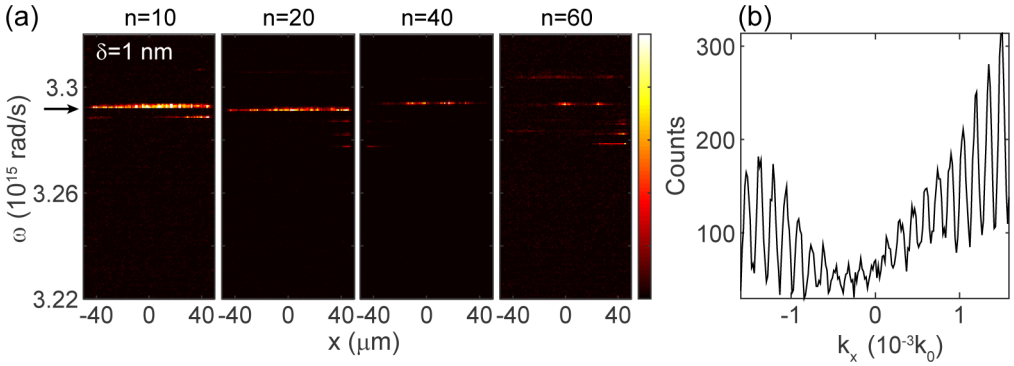

Fig. 6. (a) Measured real space spectral images of checkerboard lasers with $\delta = 1$ nm, $n = 10, 20, 40, 60$. The colorbar runs from 0 intensity to halfway the maximum intensity of each measurement. (b) Measured double slit interference of the delocalized mode(s) at 3.29×10^{15} rad/s from the $n = 10$ sample. Data are taken at maximum pump power.

Alongside the extended modes, we furthermore find that the studied lasers are surprisingly multi-mode. Both the checkerboards and random patchworks show many lasing frequencies *outside* the frequency range set by the pitches in the system, i.e., by available Bragg conditions. Figure 6(a) shows that these additional modes tend to be localized on part of the array, i.e., one or a few patches. Therefore, we found that the patchwork lasers neither lase as independent patches in an uncoupled fashion, nor purely follow that of simple extended superlattice modes. In this section, we discuss the coupling of the patches and the emergence of the multi-mode behavior.

While working out the physics for square lattices of non-linearly coupled lasers is very challenging, we look into simpler cases. We compare the spectra of a single patch from a checkerboard, and the spectra of dimers made of two adjoining square arrays. The lasing spectrum of a single patch in a checkerboard is measured by only illuminating the area within one patch of pitch 370 nm at the corner of a checkerboard array with $n = 60$. The illumination area is controlled using an iris in the path of the pump laser. As shown in Fig. 5(e) (bottom), the single patch has exactly one lasing mode, as expected from a solitary square array laser. This indicates that the multi-mode output requires more than one patch to be pumped so that at least two patches feed into each other. Further, we measured the lasing spectra of dimers of two patches that were fabricated in isolation, not as part of a larger patchwork. Each dimer contains two n =60 square arrays, one with a period of 370 nm and the other with pitch 370 nm+δ, with $\delta = 1, 2, 4$ nm. In addition to the original mode supported by a single patch, the dimers have many lasing modes at longer wavelength, as shown in Fig. 5(e). This indicates that coupling between two patches can already give rise to multi-wavelength lasing.

We explore the origin of the multi-wavelength lasing behavior from coupled wave theory, adapted from its standard form to include adjacent regions of unequal pitch. According to coupled wave theory for DFB lasers, a simple square array laser can already support multiple lasing modes at approximately equally spaced frequencies [32,33]. Each corresponds to a longitudinal lasing mode with a distinct set of frequency, threshold gain and spatial distribution. The frequency spacing between modes is expected to be inversely proportional to array size for 1D cavities [32]. Similarly, simple square 2D DFB lasers are expected to support multiple modes with a frequency spacing depending on array size. One could envision that upon coupling of patches, these single-patch longitudinal modes couple. Here we extend the coupled wave theory to coupled patches, to study whether the spatial variation in local pitch will indeed lead to new modes with

OSA CONTINUUM

different spatial distributions, frequencies and threshold gains. We implement such a model in the finite element solver COMSOL.

To set up the model, we consider 2D DFB structures with periodic variations in the x and y directions, which can be described by the scalar wave equation

$$\frac{\partial^2 E}{\partial x^2} + \frac{\partial^2 E}{\partial y^2} + k^2 E = 0 \tag{1}$$

where

$$k^2 = \beta^2 + 2i\alpha\beta + 2\beta \sum_{G\neq 0} \kappa(\mathbf{G}) e^{i\mathbf{G}.\mathbf{r}}. \tag{2}$$

Here α is the unit-cell averaged gain, $\beta = n_{\text{eff}}\omega/c$ and $\mathbf{G} = 2\pi/d(m,n)$ are the set of reciprocal lattice vectors and d is the lattice constant. For the structures studied in this work, n_{eff} corresponds to the effective refractive index of the fundamental TE waveguide mode, and the variable E represents the amplitude of excitation of this waveguide mode. 2D DFB structures have been studied in the past using coupled wave theory [34,35], assuming that the solution consists of four waves travelling in the $\pm x$ and $\pm y$ directions, at wavevectors near $\beta_0 = 2\pi/d$. We now consider two such DFB structures next to each other (placed along the x-axis) with lattice constants $d_1 = d,\ d_2 = d + \delta$ such that $\beta_1 = 2\pi/d_1$ and $\beta_2 = 2\pi/d_2$. We assume the electric field E_z to be given by the following ansatz (equal in form to that of the usual coupled wave theory, which would take β_0 in the exponent):

$$\begin{aligned} E_z = {} & R_x(x,y)e^{-i\beta_1 x} + S_x(x,y)e^{i\beta_1 x} + R_y(x,y)e^{-i\beta_1 y} \\ & + S_y(x,y)e^{i\beta_1 y}, \end{aligned} \tag{3}$$

where $R_{x,y}$ and $S_{x,y}$ represent slowly varying envelopes. Inserting the above expression in the wave equation and comparing terms with equal exponents we obtain the following set of coupled wave equations for spatial domain $i = 1, 2$ with pitch d_i

$$\begin{aligned} -\frac{\partial}{\partial x}R_x + (\alpha - i\delta_\beta)R_x = {} & i\kappa_2 S_x e^{-2i\Delta\beta_i x - 2i\phi_i} \\ & + i\kappa_{1,1} S_y e^{-i\Delta\beta_i x - i\Delta\beta_i y - i\phi_i} + i\kappa_{1,1} R_y e^{-i\Delta\beta_i x + i\Delta\beta_i y - i\phi_i} \end{aligned} \tag{4a}$$

$$\begin{aligned} \frac{\partial}{\partial x}S_x + (\alpha - i\delta_\beta)S_x = {} & i\kappa_2 R_x e^{2i\Delta\beta_i x + 2i\phi_i} \\ & + i\kappa_{1,1} S_y e^{i\Delta\beta_i x - i\Delta\beta_i y + i\phi_i} + i\kappa_{1,1} R_y e^{i\Delta\beta_i x + i\Delta\beta_i y + i\phi_i} \end{aligned} \tag{4b}$$

$$\begin{aligned} -\frac{\partial}{\partial x}R_y + (\alpha - i\delta_\beta)R_y = {} & i\kappa_2 S_y e^{-2i\Delta\beta_i y} \\ & + i\kappa_{1,1} S_x e^{-i\Delta\beta_i x - i\Delta\beta_i y - i\phi_i} + i\kappa_{1,1} R_x e^{i\Delta\beta_i x - i\Delta\beta_i y + i\phi_i} \end{aligned} \tag{4c}$$

$$\begin{aligned} \frac{\partial}{\partial x}S_y + (\alpha - i\delta_\beta)S_y = {} & i\kappa_2 R_y e^{-2i\Delta\beta_i y} \\ & + i\kappa_{1,1} S_x e^{-i\Delta\beta_i x + i\Delta\beta_i y - i\phi_i} + i\kappa_{1,1} R_x e^{i\Delta\beta_i x + i\Delta\beta_i y + i\phi_i}. \end{aligned} \tag{4d}$$

Here $\Delta\beta_i = \beta_i - \beta_0$ quantifies the spatial beat frequency between the ansatz and the actual periodicity, while ϕ_i allows for a phase jump between the two regions wich occurs upon spatially shifting the patches apart. In our implementation, $\Delta\beta_1 = 0$ and $\phi_1 = 0$. In the derivation of this equation we have assumed $(\beta^2 - \beta_i^2)/2\beta \approx \beta - \beta_i$. We focus on small frequency deviations from the geometric Bragg conditions and introduce $\kappa_{1,1} = \kappa(\mathbf{G})_{|\mathbf{G}|=\sqrt{2}\beta_1}$ and $\kappa_2 = \kappa(\mathbf{G})_{|\mathbf{G}|=2\beta_1}$. The boundary conditions are $R_x(x = -2L) = S_x(x = +2L) = R_y(y = -L) = S_y(L) = 0$ (where L is the size of a single patch). COMSOL provides eigenvalues $(\alpha - i\delta_\beta)$ that correspond to threshold gain

OSA CONTINUUM

(α) and frequency detuning (δ_β) from the geometrical Bragg condition, and eigenfunctions that indicate the intensity distribution. From standard coupled wave theory, lasers can be classified as either undercoupled ($|\kappa_2|L \ll 1$ - note that only the dimensionless product is relevant) or overcoupled ($|\kappa_2|L \gg 1$). Recent work on plasmon array lasers shows that both regimes can be reached, where the smallest patches ($n = 10, 20$) are undercoupled when viewed in isolation, but where the largest patches and the full array ($n = 60$ to $N = 240$) with $\delta = 0$ pitch variation can be overcoupled.

In the following, we discuss simulation results for the two cases: $|\kappa_2|L = 0.2$ (Fig. 7(a-c), undercoupled) and (d-f) $|\kappa_2|L = 2$ (Fig. 7(d-f), marginally overcoupled). We follow Ref. [34] in assuming $\kappa_{1,1} \approx \kappa_2/2$ and taking real coupling constants (we find similar results for complex coupling constants). A main challenge is to sort out physical eigenvalues from spurious results due to the COMSOL discretization grid. To avoid this problem, we simulate small patches ($L = 5$ μm). We show the field profiles of the three lowest threshold characteristic modes of the dimers in Fig. 7. Figure 7(a) shows the case of undercoupled patches with identical periodicities, which are effectively a single rectangular patch. We find that the dominant modes have similar profiles along the long axis as undercoupled 1D DFB lasers, with intensity located in lobes at the sample edges. Different modes arise with different number of intensity pockets along the short axis. Compared to a single square patch, the threshold gain is about twice lower, commensurate with the fact that the rectangle is twice longer. These modes have similar threshold gain, when the patches are detuned in pitch or shifted as shown in Fig. 7(b-c). This numerical result is consistent with our observation that many modes arise with closely spaced frequencies. Each of them is extended over the entire array, with different in-plane mode profiles in the y direction. This result is quite insensitive to whether the two pitches have identical or slightly different pitch variation. For large κL, the lowest threshold mode for a dimer of identical adjacent patches is overcoupled as shown in Fig. 7(d). However the next two higher order modes are undercoupled and require significantly larger threshold gain. Thus in the overcoupled case, single mode lasing is expected for identical-dimer with a threshold lower than that of an isolated single patch by about a factor 0.75. When the pitch difference is set to be 4 nm (Fig. 7(e)), all modes take a penalty in threshold gain. The resulting modes all have similar threshold gain and dominantly reside in one of the two patches, even though some amplitude is found in the neighboring patch. The mode patterns suggest that the original overcoupled mode is frustrated sufficiently by a small change in pitch to disappear. The mode distributions can be viewed as hybridized, marginally undercoupled modes of the original square patches. Similar results are found for dimers with a phase slip as shown in Fig. 7(f).

While simulations that capture the full complexity are outside the scope of our simulation framework, the quantitative picture that emerges from the dimer simulation can be summarized as follows. When a large square laser ($N = 240$ particles across) is separated in patches of detuned pitch, it fragments one overcoupled laser into patches that are by themselves undercoupled, while the overcoupled mode become that the entire patchwork would support becomes unfavorable due to the pitch detuning. As the undercoupled patches feed into each other and couple, there arises a plethora of modes with slightly detuned frequency. These modes are coherent across the array, but have unevenly distributed amplitudes due to defects and inhomogeneity introduced by the boundaries.

4.4. Angular distribution of emission

We evaluate the angular distribution of laser emission from measured above-threshold Fourier images. Figure 8(a) shows Fourier images of checkerboard lasers with $\delta = 1$ nm and $n = 10$, 20, 40, 60 at 60 % pump power, well above threshold and in the multi-mode lasing regime. For $n = 10$, 20 and 40, the Fourier images show quadruplets of peaks arranged as the vertices of squares around $k_x = k_y = 0$, corresponding to the calculated structure factors around $(\pm 1, 0)G$

OSA CONTINUUM

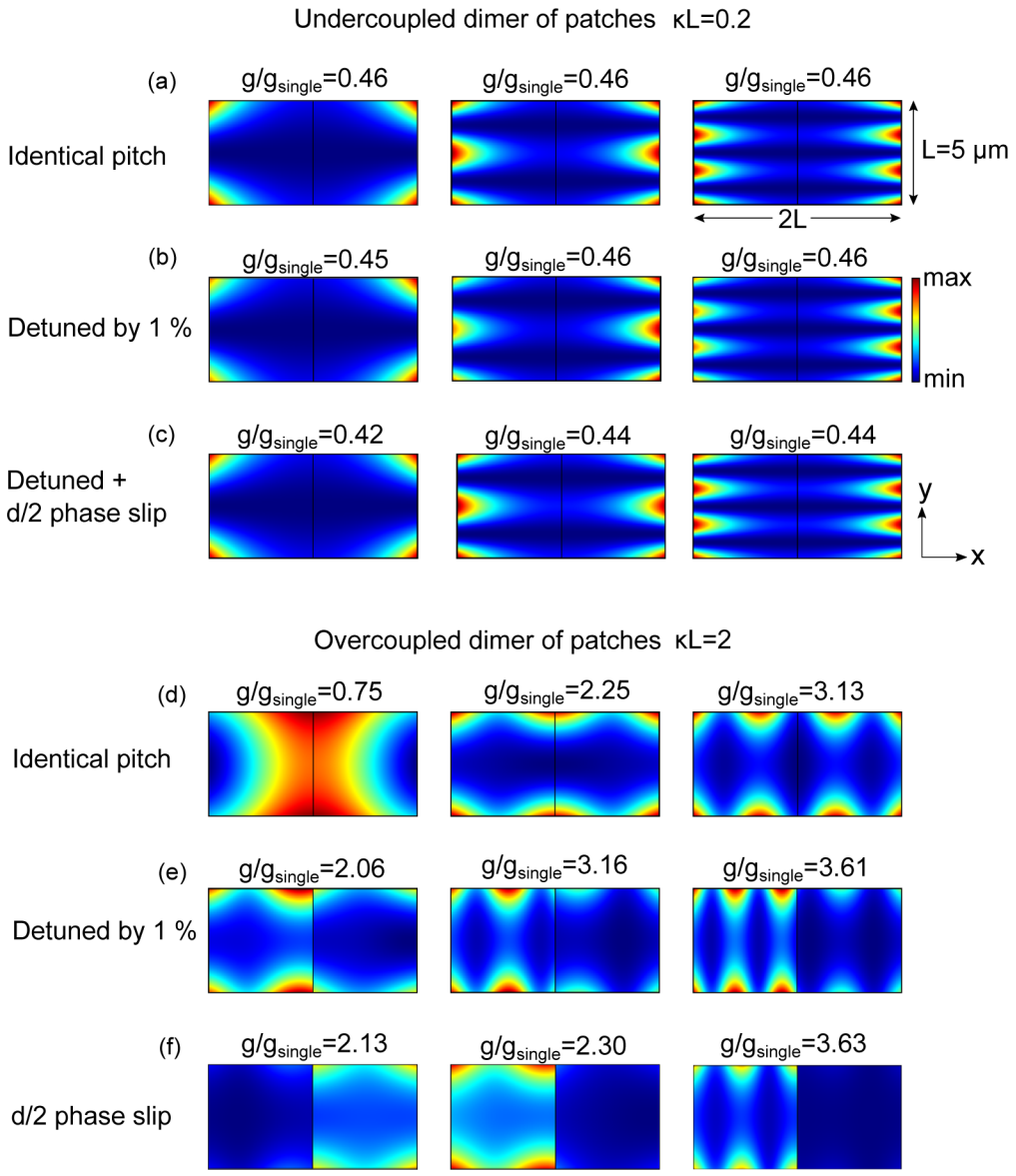

Fig. 7. COMSOL coupled wave solutions for intensity envelope functions ($|R_x|^2 + |S_x|^2 + |R_y|^2 + |S_y|^2$, normalized) in dimers of square patches in the case of (a-c) undercoupling, $|\kappa_2|L = 0.2$ and (d-f) overcoupling, $|\kappa_2|L = 2$. The quantity g/g_{single} indicates the threshold gain normalized to that for the fundamental lasing mode of a single square patch at the same coupling strength. The threshold gain for a square patch in the case $|\kappa_2|L = 0.2$ is about 6.8 times higher than that in case of $|\kappa_2|L = 2$. The simulated patches are $L = 5 \times 5$ μm across, making the dimer maps 10×5 μm^2. The color scale spans in panels (a-c) from 0 to the maxima of each image, and in panels (d-f) from the minima to the maxima, where the minima are at fractions (d) 0.25, 0.32,0.13, (e) 0.23, 0.12, 0.10, (f) 0.09, 0.07, 0.03 of the maxima. The "phase slip" cases (c,f) are pertinent for a shift of one patch relative to the other by a half pitch, as is effectively the case of our samples.

OSA CONTINUUM

and $(0, \pm 1)G$ in Fig. 2(b-c). These lasing modes at large wavevectors are coupled out through the Bragg diffractions of order $(\pm 1, 0)G$ and $(0, \pm 1)G$. With increasing n, the lasing peaks shift towards $k_x = k_y = 0$ and become indistinguishable for $n = 60$. Similar results are measured from checkerboard lasers with $\delta = 2, 4$ nm. The fact that the Fourier images follow the structure factor of the entire checkerboard directly attests to the fact that lasing modes are coherent across the entire array. Averaging the intensity in rings of constant azimuthal angles, we obtain the per solid angle (Ω) intensity distribution versus polar angle θ from the normal direction, as shown in Fig. 8(b). When $n = 10$, the checkerboard laser mainly emit at $\theta \sim 0.1$ rad, i.e., 6°. As n increases, the main emission angle decreases and converges to the normal direction. Figure 8(c) shows the above threshold Fourier images of random patchwork lasers with δ_{ij}<10 nm and $n = 10$, 20, 40, 60. As with the checkerboards, the Fourier images clearly resemble the array structure factors in Fig. 3. Figure 8(d) shows the corresponding lasing intensity distribution as a function of θ. When $n = 10$, the laser emission spans over a large angle range of ±10°. The angle range decreases with increasing n. These findings are consistent with the notion that lasing modes are extended over the entire random patchwork, and inherit their output wave vector distribution upon diffractive outcoupling.

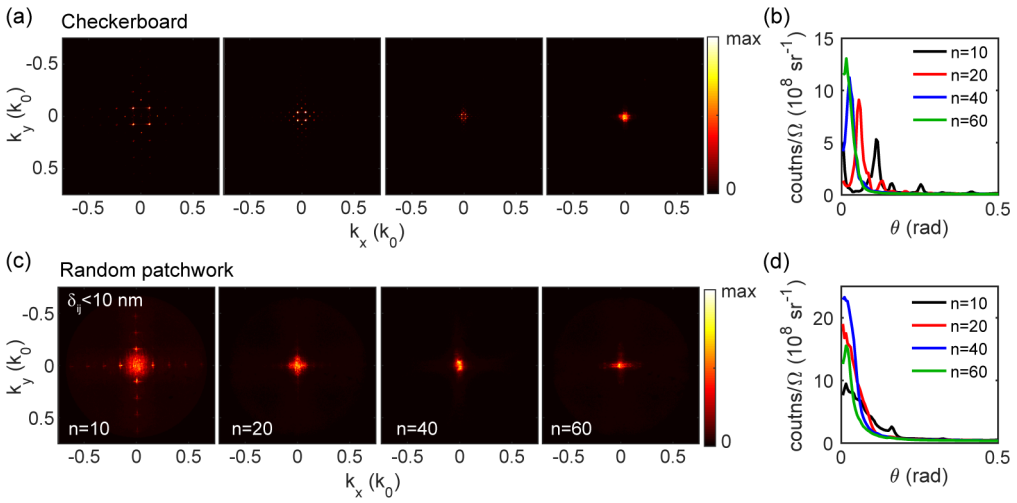

Fig. 8. (a) Above-threshold Fourier images of checkerboard lasers with $\delta = 1$ nm and $n = 10, 20, 40, 60$ excited at 60 % pump power and measured after an OD 1 filter. (b) Intensity distribution as a function of polar angle θ obtained from (a) by averaging over the azimuthal angle. (c) Measured above-threshold Fourier images of random patchwork lasers with δ_{ij}<10 nm and $n = 10, 20, 40, 60$ at 50 % pump power. (d) Intensity distribution as a function of θ obtained from (c). The Fourier images are normalized to the maxima of each image.

5. Outlook on relevance to low-etendue sources

We studied two types of plasmon DFB lasers, i.e., checkerboard and random patchwork lasers, as potential multi-wavelength, low etendue, speckle free light sources for the applications of SSL and projection. Here we discuss the implications of our observations for low-etendue bright sources in terms of three aspects: etendue, speckle reduction and output power. Our observations indicate multi-wavelength lasing emission into narrow angular cones relative to the normal direction, with modest thresholds, which are about 2 times of those of a rectangular array laser with a similar size, and similar to thresholds of polymer DFB lasers [20]. The Fourier space output as well as the thresholds indicate that the lasers support modes extending over several, or

OSA CONTINUUM

all patches of the array. Therefore, the angular output is essentially tailorable by the structure factors n and d. Measurements on dimer lasers show that a system as simple as two coupled neighboring patches already gives rise to the remarkable multimode character of our lasers. From the viewpoint of low etendue, yet broadened emission bandwidth compared to single-period large DFB lasers, these structures could thus be potentially useful for blue-LED or blue-laser pumped low-etendue light sources with reduced speckle compared to lasers.

To quantitatively estimate etendue, we examine the angular distribution of emission in Fig. 8(b)(c) and the source area. The areas of the investigated patchwork lasers are $A \sim (N \cdot d)^2 \approx 7885\ \mu m^2$. We estimate the emission angle range using the largest angle $\theta_{1/2}$ beyond which the intensity drops below half its maximum. With this definition, we obtain the etendues of the patchworks as listed in Table 1. The results range from 30 to 400 $\mu m^2 \cdot$ sr, decreasing with increasing n. These numbers are much lower than the etendue of typical projection systems using liquid-crystal display (LCD), digital light projection (DLP) and LED based luminescent concentration techniques, which are around 8 to 25 $mm^2 \cdot$ sr [36,37]. The low etendue arises from the combination of a small emission angular range, and the micron size of arrays.

Table 1. Angle at the half maximum ($\theta_{1/2}$) and etendue of the checkerboard and random patchwork lasers estimated from the angular intensity distribution in Fig. 8(b)(d).

Checkerboard, δ = 1 nm				
n	10	20	40	60
$\theta_{1/2}$ (degree)	7.2	3.7	2.0	2.3
Etendue ($\mu m^2 \cdot$sr)	389	105	30	40
Random patchwork, $\lvert\delta_{ij}\rvert$<10 nm				
n	10	20	40	60
$\theta_{1/2}$ (degree)	4.9	3.2	2.9	2.3
Etendue ($\mu m^2 \cdot$sr)	179	75	62	40

As for speckle reduction, our lasers benefit from the multiple lasing modes. Speckle consists of a random arrangement of minima and maxima with 100 % intensity contrast (truly dark spots) when a monochromatic light is scattered off a rough surface, e.g., a projection screen. Speckle contrast can be reduced by using a set of mutually incoherent modes that give uncorrelated speckle patterns. When averaging N completely uncorrelated speckle patterns, the speckle contrast is reduced by $1/\sqrt{N}$ [6]. For our plasmon patchwork lasers, the best-case estimate for their speckle reduction qualities is obtained by assuming that each laser line gives a speckle pattern that is completely uncorrelated from that of other lines. For our lasers with a typical multimode behavior of up to 15 lines, a speckle contrast of 25 % remains when all the modes are uncorrelated and contribute equally in intensity. However, speckle patterns generated from the scattering of close illumination frequencies off a random medium can be correlated [38,39], unless the involved path length differences exceed the coherence length [40]. The bandwidth of our plasmon patchwork lasers spans up to about 15 nm, i.e., about 2.5 % relative bandwidth, corresponding to a 22 micron coherence length. This coherence length is only slightly larger than typical diffusive media such as white paint and white paper, which have a mean free path between 4 μm (paint) [41] and 20 μm (paper) [42]. Therefore, the multi-wavelength emission from our lasers can indeed be useful for speckle reduction both when considering reflection and tranmission off/through a screen.

A distinct challenge of these structures is to obtain high power outputs, because of the small emission volume and high photodegradation. Only select fluorophores offer stability against bleaching and overheating at high pump power and no such fluorophore has been proposed yet for plasmon-array lasers. The efficiency of color conversion is limited by three factors: absorption of the pump light (at best 35%, limited by the 350 nm thickness of our films and

OSA CONTINUUM

the dye concentration), Ohmic loss in the metal particles and the extraction efficiency of the emitted light (50% maximum in our structures). Therefore, our investigated lasers would have a quantum efficiency no higher than 17.5%, assuming negligible Ohmic loss. More fundamentally, for applications that require up to 1000 lumen, the emission volume itself is limiting. At dye concentrations where concentration quenching sets in, one could maximally obtain of order 1 lm/μm^2 for a wavelength of 570 nm from a thin film continuously operated in saturation. Even if the required area to reach 1000 lm is not unphysical in itself, this would involve very high heat dissipation of about 10^{-5} W $\cdot$ μm^{-2} from the Stokes shift, which can not be sustained by such a thin film. Such problems may be resolved by moving to the regime of plasmon exciton polariton lasing reported by Ramezani [21], which uses the same structure but much higher emitter concentration.

Funding

Nederlandse Organisatie voor Wetenschappelijk Onderzoek (NWO).

Acknowledgements

We thank Bob Drent and Dimitry Lamers for sample fabrication, and are grateful to Jaime Gomez Rivas, Mohammad Ramezani, Dick de Boer, Henri Jagt and Toni Lopez for discussions. Also, we thank John Mathew for his thorough review of our manuscript.

References

1. K. A. Denault, M. Cantore, S. Nakamura, S. P. DenBaars, and R. Seshadri, "Efficient and stable laser-driven white lighting," AIP Adv. **3**(7), 072107 (2013).
2. Y. H. Song, E. K. Ji, B. W. Jeong, M. K. Jung, E. Y. Kim, and D. H. Yoon, "High power laser-driven ceramic phosphor plate for outstanding efficient white light conversion in application of automotive lighting," Sci. Rep. **6**(1), 31206 (2016).
3. A. F. George, S. Al-waisawy, J. T. Wright, W. M. Jadwisienczak, and F. Rahman, "Laser-driven phosphor-converted white light source for solid-state illumination," Appl. Opt. **55**(8), 1899–1905 (2016).
4. R. Knize, "Full color solid state laser projector system," US Pat. 5,317,348 (1994).
5. B. D. Silverstein, A. F. Kurtz, J. R. Bietry, and G. E. Nothhard, "25.4: A laser-based digital cinema projector," SID Symp. Dig. Tech. Pap. **42**(1), 326–329 (2011).
6. J. W. Goodman, *Speckle phenomena in optics: theory and applications* (Roberts and Company Publishers, 2007).
7. J. I. Trisnadi, "Speckle contrast reduction in laser projection displays," Proc. SPIE **4657**, 131–137 (2002).
8. T.-T.-K. Tran, Ø. Svensen, X. Chen, and M. N. Akram, "Speckle reduction in laser projection displays through angle and wavelength diversity," Appl. Opt. **55**(6), 1267–1274 (2016).
9. E. Rawson, "Speckle minimization in projection displays by reducing spatial coherence of the image light," US Pat. 4,035,068 (1977).
10. E. G. Rawson, A. B. Nafarrate, R. E. Norton, and J. W. Goodman, "Speckle-free rear-projection screen using two close screens in slow relative motion," J. Opt. Soc. Am. **66**(11), 1290–1294 (1976).
11. L. Wang, T. Tschudi, T. Halldórsson, and P. R. Pétursson, "Speckle reduction in laser projection systems by diffractive optical elements," Appl. Opt. **37**(10), 1770–1775 (1998).
12. S. C. Shin, S. S. Yoo, S. Y. Lee, C.-Y. Park, S.-Y. Park, J. W. Kwon, and S.-G. Lee, "Removal of hot spot speckle on laser projection screen using both the running screen and the rotating diffuser," Displays **27**(3), 91–96 (2006).
13. T.-K.-T. Tran, X. Chen, Ø. Svensen, and M. N. Akram, "Speckle reduction in laser projection using a dynamic deformable mirror," Opt. Express **22**(9), 11152–11166 (2014).
14. X. Meng, J. Liu, A. V. Kildishev, and V. M. Shalaev, "Highly directional spaser array for the red wavelength region," Laser Photonics Rev. **8**(6), 896–903 (2014).
15. J. Stehr, J. Crewett, F. Schindler, R. Sperling, G. von Plessen, U. Lemmer, J. Lupton, T. Klar, J. Feldmann, A. Holleitner, M. Forster, and U. Scherf, "A low threshold polymer laser based on metallic nanoparticle gratings," Adv. Mater. **15**(20), 1726–1729 (2003).
16. J. Y. Suh, C. H. Kim, W. Zhou, M. D. Huntington, D. T. Co, M. R. Wasielewski, and T. W. Odom, "Plasmonic bowtie nanolaser arrays," Nano Lett. **12**(11), 5769–5774 (2012).
17. W. Zhou, M. Dridi, J. Y. Suh, C. H. Kim, D. T. Co, M. R. Wasielewski, G. C. Schatz, and T. W. Odom, "Lasing action in strongly coupled plasmonic nanocavity arrays," Nat. Nanotechnol. **8**(7), 506–511 (2013).
18. A. Yang, T. B. Hoang, M. Dridi, C. Deeb, M. H. Mikkelsen, G. C. Schatz, and T. W. Odom, "Real-time tunable lasing from plasmonic nanocavity arrays," Nat. Commun. **6**(1), 6939 (2015).

OSA CONTINUUM

19. A. Yang, Z. Li, M. P. Knudson, A. J. Hryn, W. Wang, K. Aydin, and T. W. Odom, "Unidirectional lasing from template-stripped two-dimensional plasmonic crystals," ACS Nano **9**(12), 11582–11588 (2015).
20. A. H. Schokker and A. F. Koenderink, "Lasing at the band edges of plasmonic lattices," Phys. Rev. B **90**(15), 155452 (2014).
21. M. Ramezani, A. Halpin, A. I. Fernández-Domínguez, J. Feist, S. R.-K. Rodriguez, F. J. García-Vidal, and J. G. Rivas, "Plasmon-exciton-polariton lasing," Optica **4**(1), 31–37 (2017).
22. T. K. Hakala, H. T. Rekola, A. I. Väkeväinen, J.-P. Martikainen, M. Nečada, A. J. Moilanen, and P. Törmä, "Lasing in dark and bright modes of a finite-sized plasmonic lattice," Nat. Commun. **8**(1), 13687 (2017).
23. H. T. Rekola, T. K. Hakala, and P. Törmä, "One-dimensional plasmonic nanoparticle chain lasers," ACS Photonics **5**(5), 1822–1826 (2018).
24. K. S. Daskalakis, A. I. Väkeväinen, J.-P. Martikainen, T. K. Hakala, and P. Törmä, "Ultrafast pulse generation in an organic nanoparticle-array laser," Nano Lett. **18**(4), 2658–2665 (2018).
25. A. H. Schokker and A. F. Koenderink, "Statistics of randomized plasmonic lattice lasers," ACS Photonics **2**(9), 1289–1297 (2015).
26. A. H. Schokker and A. F. Koenderink, "Lasing in quasi-periodic and aperiodic plasmon lattices," Optica **3**(7), 686–693 (2016).
27. D. Wang, A. Yang, W. Wang, Y. Hua, R. D. Schaller, G. C. Schatz, and T. W. Odom, "Band-edge engineering for controlled multi-modal nanolasing in plasmonic superlattices," Nat. Nanotechnol. **12**(9), 889–894 (2017).
28. G. Lozano, D. J. Louwers, S. R. Rodriguez, S. Murai, O. T. Jansen, M. A. Verschuuren, and J. Gómez Rivas, "Plasmonics for solid-state lighting: enhanced excitation and directional emission of highly efficient light sources," Light: Sci. Appl. **2**(5), e66 (2013).
29. G. Lozano, S. R. K. Rodriguez, M. A. Verschuuren, and J. G. Rivas, "Metallic nanostructures for efficient LED lighting," Light: Sci. Appl. **5**(6), e16080 (2016).
30. A. H. Schokker, F. van Riggelen, Y. Hadad, A. Alú, and A. F. Koenderink, "Systematic study of the hybrid plasmonic-photonic band structure underlying lasing action of diffractive plasmon particle lattices," Phys. Rev. B **95**(8), 085409 (2017).
31. K. Guo, M. Du, C. I. Osorio, and A. F. Koenderink, "Broadband light scattering and photoluminescence enhancement from plasmonic vogel's golden spirals," Laser Photonics Rev. **11**(3), 1600235 (2017).
32. H. Kogelnik and C. V. Shank, "Coupled-wave theory of distributed feedback lasers," J. Appl. Phys. **43**(5), 2327–2335 (1972).
33. K. Sakai, E. Miyai, and S. Noda, "Coupled-wave theory for square-lattice photonic crystal lasers with te polarization," IEEE J. Quantum Electron. **46**(5), 788–795 (2010).
34. K. Sakai, E. Miyai, and S. Noda, "Two-dimensional coupled wave theory for square-lattice photonic-crystal lasers with tm-polarization," Opt. Express **15**(7), 3981–3990 (2007).
35. M. P. van Exter, V. T. Tenner, F. van Beijnum, M. J. A. de Dood, P. J. van Veldhoven, E. J. Geluk, and G. W. 't Hooft, "Surface plasmon dispersion in metal hole array lasers," Opt. Express **21**(22), 27422–27437 (2013).
36. G. Derra, H. Moench, E. Fischer, H. Giese, U. Hechtfischer, G. Heusler, A. Koerber, U. Niemann, F.-C. Noertemann, P. Pekarski, J. Pollmann-Retsch, A. Ritz, and U. Weichmann, "Uhp lamp systems for projection applications," J. Phys. D: Appl. Phys. **38**(17), 2995–3010 (2005).
37. D. K. G. de Boer, D. Bruls, and H. Jagt, "High-brightness source based on luminescent concentration," Opt. Express **24**(14), A1069–A1074 (2016).
38. C. A. Thompson, K. J. Webb, and A. M. Weiner, "Diffusive media characterization with laser speckle," Appl. Opt. **36**(16), 3726–3734 (1997).
39. A. P. Mosk, A. Lagendijk, G. Lerosey, and M. Fink, "Controlling waves in space and time for imaging and focusing in complex media," Nat. Photonics **6**(5), 283–292 (2012).
40. O. L. Muskens, T. van der Beek, and A. Lagendijk, "Angle dependence of the frequency correlation in random photonic media: Diffusive regime and its breakdown near localization," Phys. Rev. B **84**(3), 035106 (2011).
41. P. M. Johnson, T. van der Beek, and A. Lagendijk, "Diffuse imaging and radius dependent frequency correlations in strongly scattering media," Opt. Express **22**(11), 13330–13342 (2014).
42. A. Badon, D. Li, G. Lerosey, A. C. Boccara, M. Fink, and A. Aubry, "Smart optical coherence tomography for ultra-deep imaging through highly scattering media," Sci. Adv. **2**(11), e1600370 (2016).